research papers

Performance calculations of the X-ray powder diffraction beamline at NSLS-II

Xianbo Shi,[a] Sanjit Ghose[b] and Eric Dooryhee[b]*

[a]European Synchrotron Radiation Facility, 6 rue Jules Horowitz, Grenoble 38043, France, and [b]Photon Sciences Directorate, Brookhaven National Laboratory, PO Box 5000, Upton, NY 11973, USA. E-mail: edooryhee@bnl.gov

The X-ray Powder Diffraction (XPD) beamline at the National Synchrotron Light Source II is a multi-purpose high-energy X-ray diffraction beamline with high throughput and high resolution. The beamline uses a sagittally bent double-Laue crystal monochromator to provide X-rays over a large energy range (30–70 keV). In this paper the optical design and the calculated performance of the XPD beamline are presented. The damping wiggler source is simulated by the *SRW* code and a filter system is designed to optimize the photon flux as well as to reduce the heat load on the first optics. The final beamline performance under two operation modes is simulated using the *SHADOW* program. For the first time a multi-lamellar model is introduced and implemented in the ray tracing of the bent Laue crystal monochromator. The optimization and the optical properties of the vertical focusing mirror are also discussed. Finally, the instrumental resolution function of the XPD beamline is described in an analytical method.

1. Introduction

An X-ray Powder Diffraction (XPD) beamline is being built at the new synchrotron X-ray source (NSLS-II) at Brookhaven National Laboratory, USA. The optical scheme takes full advantage of the high flux of a 7 m-long 1.8 T damping wiggler, and uses techniques and instrumentation pioneered or under development at the NSLS [*e.g.* Laue optics (Zhong *et al.*, 2001*a*,*b*) and Ge strip array detectors (Rumaiz *et al.*, 2010)]. Using three experimental hutches, the XPD powder diffraction beamline will be a multi-instrument facility with the ability to collect diffraction data at high monochromatic X-ray energies (30–70 keV), offering rapid acquisition (sub-second) as well as high angular resolution capabilities. XPD is designed to combine high Q-space resolution diffraction measurements and high real-space resolution pair distribution function (PDF) measurements. The beam size is adjustable to match the graininess and heterogeneity scales of the samples above the micrometer scale. XPD addresses future scientific challenges in, for example, hydrogen storage, CO_2 sequestration, advanced structural ceramics, catalysis and materials processing. Such materials of high technological value often are complex, nanostructured and heterogeneous. The scientific grand challenge is to obtain robust and quantitative (micro)structural information, not only in the ground state under ambient conditions but also *in situ* or *in operando* with varying temperature, pressure, magnetic, electric or stress

field, chemical environment, *etc*. The XPD beamline will be commissioned during 2014 and full user operation mode is due to begin in June 2015.

This paper describes the layout and calculates the expected performance of the XPD beamline. The source simulation and the beamline ray tracing are performed using the *SRW* (Chubar, 2001) program and the *SHADOW* (Welnak *et al.*, 1994) code under *XOP* (Sanchez del Rio & Dejus, 2004). In particular, we developed a multi-lamellar model to simulate the performance of the sagittally bent double-Laue crystal monochromator (DLM). The instrumental resolution function (IRF) of the XPD beamline is expressed in an analytical method, which includes the contributions from each optical element of the beamline.

The purpose is first to rationalize and optimize the choice of each optical component of the XPD beamline. The simulated performance will be useful for future users to explore the capabilities of the beamline as well as to plan for early experiments. At the same time, the simulation method (*e.g.* the multi-lamellar modelling of the DLM and the IRF calculation) shown in this work will also benefit the design of high-energy wiggler beamlines in the future.

2. Beamline layout/description

The XPD beamline is designed to operate under two different operation modes, *i.e.* the high-flux mode and the high-reso-
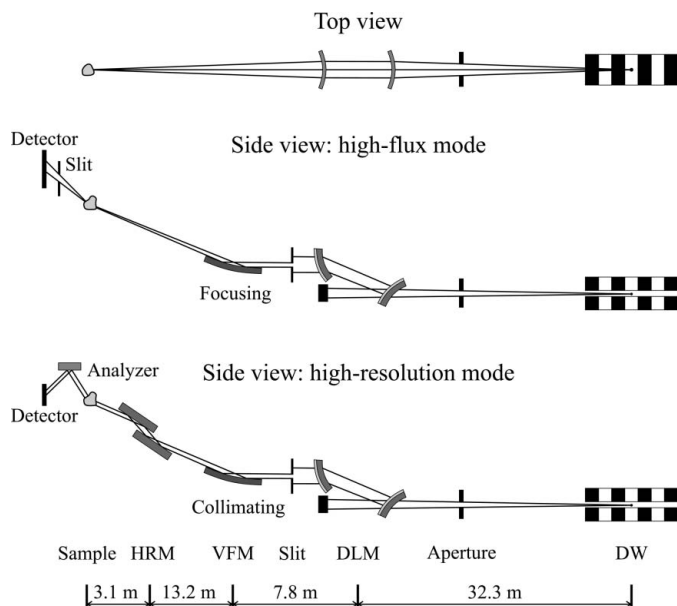
Top view

Detector
Slit
Side view: high-flux mode

Focusing

Analyzer
Detector
Side view: high-resolution mode

Collimating

Sample   HRM   VFM   Slit   DLM   Aperture   DW

|— 3.1 m —|— 13.2 m —|— 7.8 m —|——— 32.3 m ———|

Figure 1
Schematic layout of the XPD beamline. DW: damping wiggler; DLM: double-Laue crystal monochromator; VFM: vertical focusing mirror; HRM: high-resolution monochromator.

lution mode. The optical layouts are shown in Fig. 1. In the high-flux mode the X-ray beam generated by the damping wiggler is horizontally focused by the sagittally bent DLM and vertically focused by the vertical focusing mirror (VFM). The modest 0.1% energy bandwidth is acceptable for many high-energy experiments, *e.g. in situ*, time-resolved, materials science, strain and stress analysis, and PDF research. In the high-resolution mode the beam is collimated by the VFM in the vertical diffraction plane before impinging a channel-cut high-resolution monochromator (HRM). Both the induced lower vertical divergence and the higher monochromaticity ($\Delta E/E \simeq 10^{-4}$) improve the resolution performance for such experiments as structure solving, lattice parameter measurement and line shape analysis.

3. Performance calculations

The beamline parameters for all the XPD optical elements are listed in Table 1.

3.1. Incident beam properties

The damping wiggler source (DW100) is located in a high-β straight section of the NSLS-II storage ring. The DW100 extends the range of X-ray energies well beyond 50 keV, thus matching the scientific needs of the XPD beamline. The total power generated by the DW100 is 61 kW when the NSLS-II ring electron beam current reaches the nominal value of 500 mA [see Fig. 2(a) for the power density distribution]. The XPD beamline accepts 1.1 mrad horizontally and 0.1 mrad vertically from the DW100 radiation using a fixed aperture mask, within which the total power is 5.9 kW. Most of the

Table 1
Beamline parameters.

Damping wiggler (DW100)	
Number of periods	68
Period length (mm)	100
Effective K value, K_{eff}	16.5
Electron beam size r.m.s (μm)	137×4.9
Electron beam divergence r.m.s (μrad)	6.6×1.6
Fixed mask aperture (mrad)	1.1×0.1
Filter assembly from source (m)	30
DLM	
Distance from source, F_1 (m)	32.3
Vertical offset (mm)	50
Crystal orientation	111 reflection on Si (100) crystal
Crystal asymmetric angle, χ (°)	35.26
Crystal thickness, T_0 (mm)	0.7
Range of R_s (m)†	0.8–∞
Mirror	
Distance from source, p (m)	40.1
Grazing angle, δ (mrad)†	1.0–2.0
Bending radius, R (km)†	12–76
Mirror length, L (mm)	1300
HRM	
Distance from source (m)	53.3
Crystal orientation	Symmetric Si (111) crystal
Sample-to-source distance (m)	56.4

† The value depends on the operation energy (see Table 2 and Fig. 9 for details).

thermal power of the DW100 lies inherently within the low-energy spectrum (50% occurs below the critical energy of 11.1 keV). The XPD beamline uses two fixed diamond filters
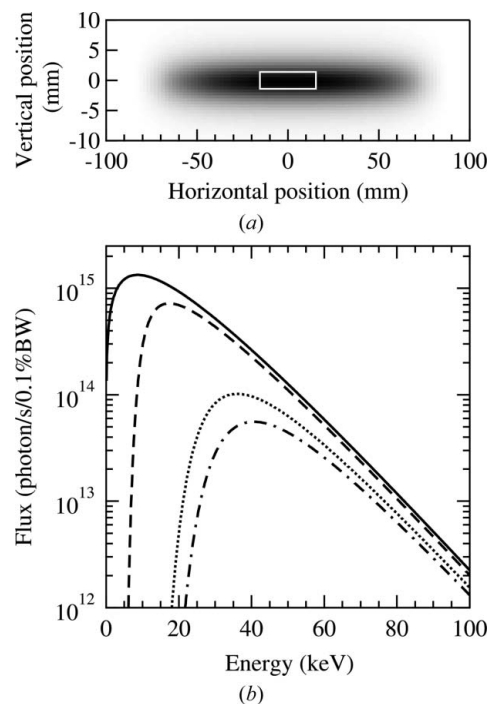

Figure 2
(a) Power density of the damping wiggler source (DW100) at 28 m from the source, calculated using *SRW* (Chubar, 2001). The gray color scale represents the power density, ranging from zero (white) to the on-axis power density of 72 W mm^{-2} (black). The white box denotes the fixed mask aperture of 1.1 mrad $\times$ 0.1 mrad. (b) Power spectrum within the fixed aperture of the source (solid line), the beam after 2 mm of diamond (dashed line), and the beam after 2 mm of diamond and 4.8 mm of SiC (dotted line) or 8 mm of silicon carbide (dash-dotted line).

(one also serves as a vacuum isolation window) and one set of adjustable silicon carbide (SiC) filters to attenuate the beam. This concept is being successfully used at the I12 beamline at Diamond Light Source (Drakopoulos, 2010). Fig. 2(b) shows the power spectrum of the incident beam after 2 mm of diamond and different thicknesses of SiC. The diamond filter, which could consist of a single 2 mm-thick window, will be made for safety reasons of two 1 mm-thick windows. The SiC is subdivided into five filters to modulate the amount of transmitted power to allow as low as 0.28 kW (with the maximum of 8 mm of SiC filters in the beam) incident on the first white-beam optics (DLM). All subsequent calculations are based on the optimized case when 2 mm of diamond and 4.8 mm of SiC are applied [see Fig. 2(b) for the power spectrum].

Fig. 3 shows the angular profiles of the DW100 emission at different energies as calculated by *SRW* and *SHADOW*. The 0.1 mrad aperture in the vertical plane matches the angular acceptance of the vertical focusing mirror. As a result, the profiles of the X-ray beam are shown in Fig. 3. Since the profiles are neither uniform nor Gaussian shapes, one has to model the emission of the full 7 m-long damping wiggler together with the fixed mask aperture. In *SHADOW*, the *EPATH* routine computes the electron trajectory in the wiggler, and then photon rays emitted at each point of the trajectory are integrated and normalized to obtain the total photon emission. The effective X-ray source size is obtained by back-tracing the output rays at the far field to the center of the wiggler. The X-ray source r.m.s. size is calculated to be 650 µm × 54 µm with a mask aperture size of 1.1 mrad × 0.1 mrad [cf. Fig. 4(a)]. The effective source size within the 0.1 mrad fixed aperture [gray region in Fig. 4(b)] linearly varies with the size of the vertical slit. The vertical slit size should match the angular acceptance of the vertical focusing mirror. For instance, at 50 keV the mirror grazing angle is 1.5 mrad to ensure total reflection. For a 1.3 m-long mirror the vertical acceptance is reduced to 0.05 mrad. As a result, the effective vertical source size is calculated to be 28 µm (r.m.s.).

Figure 4
(a) Effective X-ray source profile at 50 keV for a mask aperture size of 1.1 mrad × 0.1 mrad. The X-ray source r.m.s. size is 650 µm × 54 µm. (b) Effective vertical source r.m.s. size as a function of vertical aperture at 30 keV (triangles), 50 keV (circles) and 70 keV (squares).

3.2. The sagittally bent double-Laue crystal monochromator

3.2.1. Basic concept and parameters. The XPD beamline intends to use a sagittally bent double-Laue monochromator (*cf.* Fig. 5) for providing a focused and adjustable monochromatic beam with optimized flux at the sample. The DLM is most suited for high-energy powder diffraction beamlines (*e.g.* XPD) because it provides energy tunability, maximized total flux, medium energy resolution and adequate size of the beam. The focusing capability of the DLM is similar to that of the sagittal focusing by a Bragg crystal, but Laue crystals are less sensitive to the thermal load and vibration because of the smaller beam footprint and the larger angular acceptance (Suortti *et al.*, 1990). The transmission geometry is also the best choice for high-energy wiggler beamlines in terms of reducing the crystal size and easing the alignment.

The sagittally bent double-Laue crystal monochromator (Zhong *et al.*, 2001a,b) was pioneered at the National Synchrotron Light Source (NSLS). The focusing condition of the DLM is given by Zhong *et al.* (2001a),

$$1/F_1 + 1/F_2 = 4\sin\theta_m \sin\chi/R_s, \qquad (1)$$
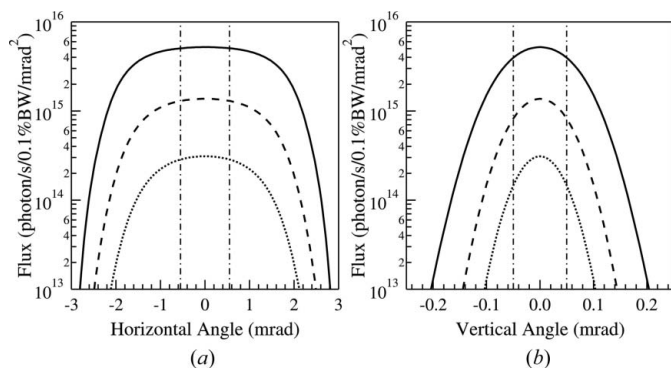

Figure 3
Angular profiles of DW100 emission at 30 keV (solid line), 50 keV (dashed line) and 70 keV (dotted line) in the horizontal (a) and the vertical (b) directions, respectively. The vertical dash-dotted lines show the angular acceptance of the fixed mask, which defines a 1.1 mrad aperture horizontally and a 0.1 mrad aperture vertically.
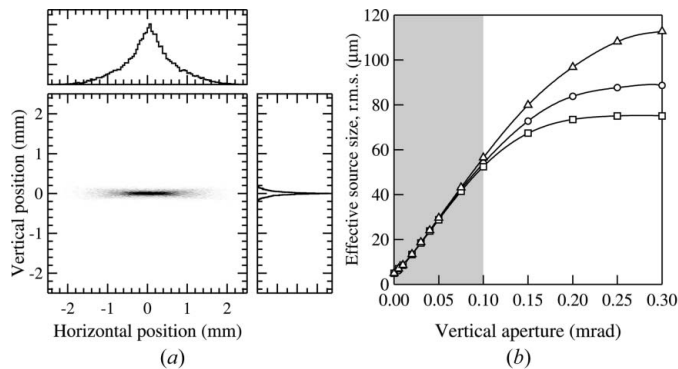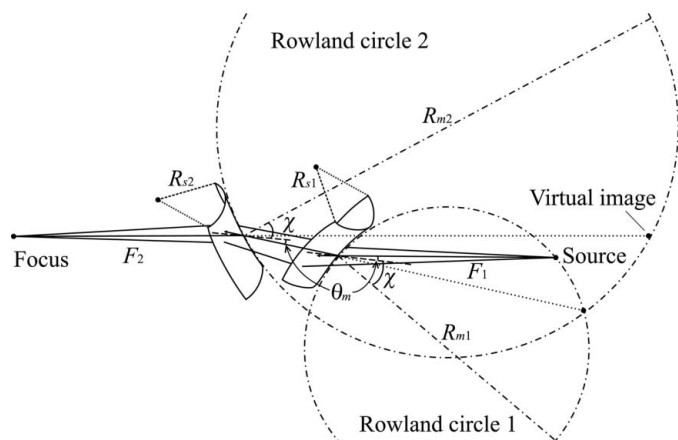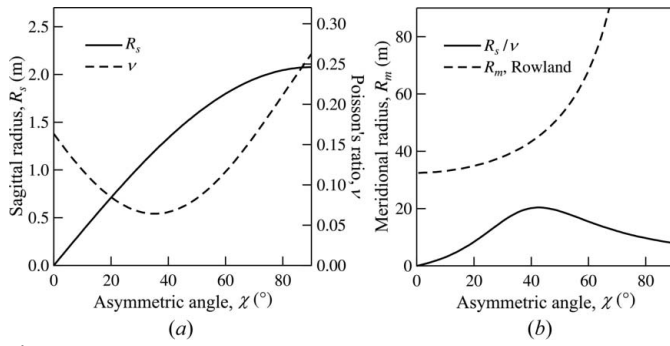

Figure 5
Schematic of the sagittally bent double-Laue crystal monochromator.

Figure 6
(a) DLM sagittal radius R_s plotted as a function of the asymmetric angle χ (solid line), the Poisson ratio ν as a function of χ in the $(0\bar{1}1)$ plane (dashed line), (b) R_s/ν and the meridional radius R_m that satisfies the Rowland condition as a function of χ at 50 keV, with the source-to-DLM distance $F_1 = 32.3$ m and the DLM-to-sample distance $F_2 = 24.1$ m.

where F_1 and F_2 are the source-to-DLM and DLM-to-sample distances (assuming the distance between the two crystals is small), respectively, θ_m is the Bragg angle of the monochromator, χ is the asymmetric angle, and R_s is the sagittal bending radius of both Laue crystals. The anticlastic (meridional) bending radius R_m is then given by $R_m = R_s/C\nu$, where ν is the Poisson ratio of the crystal for a given orientation and C is a correction term accounting for the crystal shape and the bending mechanism (Zhong *et al.*, 2002; Krisch *et al.*, 1991).

Fig. 6(a) presents the sagittal radius R_s needed for the horizontal focusing as a function of χ obtained from (1). χ should not be too small ($>20°$), so as not to break the crystal. The Poisson ratio ν is highly dependent on the crystal orientation owing to the anisotropy of silicon (Wortman & Evans, 1965). Fig. 6(a) also shows ν as a function of χ in the $(0\bar{1}1)$ plane. As a result, R_s/ν (knowing that R_m is proportional to R_s/ν) achieves the maximum at $\chi \simeq 40°$ [see the solid line in Fig. 6(b)]. Considering that the required R_m for the Rowland condition [see the dashed line in Fig. 6(b)] is given by

$$R_m = F_1/\gamma_0, \qquad (2)$$

with the direction cosine of the incident beam $\gamma_0 = \cos(\chi + \theta_m)$ for the XPD geometry, one finds that the value χ where R_s/ν and R_m (Rowland condition) are the closest is about 35°. This optimized χ can be obtained by using the 111 reflection on the (100) crystal ($\chi = 35.26°$). Once the asymmetric angle is chosen, the actual R_m is then a function of the parameter C, which can be experimentally determined or calculated using finite-element analysis (Shi *et al.*, 2011). This drives the choice of the crystal dimensions (*i.e.* length, width and thickness) and of the bender design.

The rocking curve width, ω_0, of the sagittally bent crystal is given by (Zhong *et al.*, 2002, 2003)

$$\omega_0 \cong \left[\Delta\theta^2(T_0) + \omega_a^2\right]^{1/2}, \qquad (3)$$

where T_0 is the thickness of the crystal and ω_a is the Darwin width for a given material and Bragg reflection. $\Delta\theta(T_0)$ is the total change of Bragg condition caused by lattice distortion, and is given by

$$\begin{aligned} \Delta\theta(T_0) = (T_0/R_s)\Big\{ &-\Big[(S'_{13} - CS'_{23})\sin\chi\cos\chi \\ &- CS'_{23}\tan(\chi + \theta_m) + S'_{63}\cos^2\chi\Big] \\ &- \tan\theta_m\Big[S'_{13}\sin^2\chi + CS'_{23}\cos^2\chi \\ &+ S'_{63}\sin\chi\cos\chi\Big]\Big\}, \end{aligned} \qquad (4)$$

where $S'_{ij} = S_{ij}/S_{33}$, and S_{ij} are the elastic compliances of the crystal (the Poisson ratio is $\nu = -S'_{23}$ in the above equation). Since the total distortion $\Delta\theta(T_0)$ is proportional to the crystal thickness T_0, one has to increase the crystal thickness in order to achieve high flux to the detriment of energy resolution. However, increasing the thickness also induces more stress in the crystal up to the breaking point.

3.2.2. Shadow ray-tracing with the multi-lamellar approach. The rocking curves of sagittally bent Laue crystals can be simulated within the dynamical theory (*e.g.* the multi-lamellar approximation, the Penning–Polder method and the Takagi–Taupin theory) once the anisotropy of the crystal is implemented (Shi, 2011). The total angle change $\Delta\theta(T_0)$ is a result of two terms: (i) the change of the lattice orientation through the crystal thickness, and (ii) the angle change owing to the lattice spacing variation. For a sagittally bent Laue crystal, the former effect is one magnitude larger than the latter one. To include these effects, the DLM was ray-traced using *SHADOW* by dividing the bent Laue crystal into n thin lamellae with a thickness of ΔT. The Bragg plane in each lamella is tilted by an angle relative to the Bragg planes in its neighbor lamellae, that is, the asymmetric angle varies from one lamella to the next [*cf.* Fig. 7(a)]. The reflectivity and transmission of each lamella can be calculated from the dynamical theory, and the overall reflectivity of a crystal consisting of n lamellae is then (Shi, 2011)

$$\mathcal{R} = \sum_{i=1}^{n}\left\{r_i\exp\left[-\mu(n-i)L_h\right]\left(\prod_{j=1}^{i-1}t_j\right)\right\}, \qquad (5)$$

where r_i is the reflectivity of the ith lamella, t_j is the transmission of the jth lamella before the ith lamella, μ is the linear absorption coefficient, and $L_h = \Delta T/\gamma_H$ is the X-ray path of the diffracted beam through each lamella. For the XPD geometry, the direction cosine of the diffracted beam is $\gamma_H = \cos(\chi - \theta_m)$. In this work, the reflectivity and transmission of each lamella is simulated by means of *SHADOW*. The thickness of the lamella is chosen so that the tilt angle between two sequential lamellae equals the Darwin width of the perfect crystal.

Fig. 7(b) illustrates an example calculation at 50 keV for XPD. The (100) crystal, 0.7 mm thick, was sagittally bent along the $[0\bar{1}1]$ direction to a radius of 1.25 m. The corresponding R_m is 28 m with $\nu = 0.064$ and $C = 0.7$. The total distortion $\Delta\theta$ calculated from (3) is 67.6 μrad. The crystal is then divided into 15 lamellae, each of which has a thickness of 47 μm. The rocking curves of all lamellae are shown as dotted curves in Fig. 7(b). The rocking curve from each lamella is offset by 1/15 of $\Delta\theta$ from its neighbour lamella. Applying (5), the total
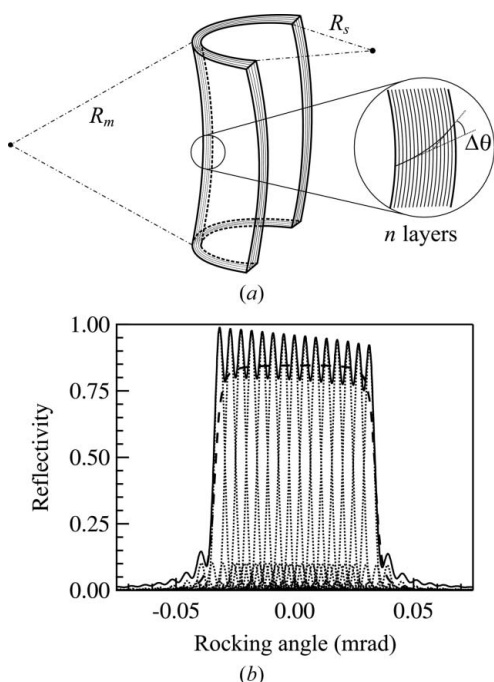
Figure 7
(*a*) Multi-lamellar model of the sagittally bent Laue crystal. (*b*) The rocking curve (solid line) of the 111 reflection on a 0.7 mm-thick (100) crystal bent to R_s = 1.25 m is constructed using equation (5) with 15 lamellae of perfect crystal (rocking curves of all lamellae are shown as dashed lines). The dashed line denotes the diffraction profile of the same crystal calculated from the Penning–Polder theory. The X-ray energy is 50 keV.

Figure 8
Beam spot simulated by *SHADOW* at the sample position (56.4 m from the source) of the XPD beamline without (*a*) and with (*b*) the DLM (located 32.3 m from the source). The X-ray beam generated by the DW100 source at 50 keV is predefined by a fixed aperture of 1.1 mrad × 0.1 mrad. See the caption of Fig. 7 for the crystal parameters.

rocking curve is constructed as the solid curve in Fig. 7(*b*). The result agrees with the diffraction profile calculated from the Penning–Polder theory (Shi, 2011) [dashed line in Fig. 7(*b*)]. This multi-lamellar approach using *SHADOW* ray tracing is applicable when the multi-lamellar approximation remains valid (Shi, 2011).

For the conventional meridionally bent double-Laue crystal monochromator, the surfaces of the two crystals are parallel. The geometric effect in the diffraction plane caused by the first crystal is cancelled out by the second crystal. Therefore, the virtual image after both crystals coincides with the source when the distance between the two crystals is negligible. However, for the sagittally bent DLM, the virtual image-to-crystal distance will be multiplied by a factor of γ_H^2/γ_0^2 when the Rowland condition is achieved for both crystals (*cf.* Fig. 5). Similarly, the vertical height of the exit beam is altered by the same factor. The vertical divergence of the beam is also modified by the angular width of the crystal diffraction profile. As a result, the focusing condition and the beam size in the vertical direction cannot be calculated easily with an analytical approach but with the ray tracing (*e.g. SHADOW*). Fig. 8 shows the beam size dimension simulated at the sample position without and with the DLM at 50 keV for the XPD geometry. In the horizontal plane, the beam is focused from a near-uniform distribution with a width of 62 mm (*cf.* Fig. 3) to a Gaussian-shaped profile with a FWHM of 0.6 mm. On the other hand, a detectable increase of the vertical beam size is observed following the effects mentioned above.
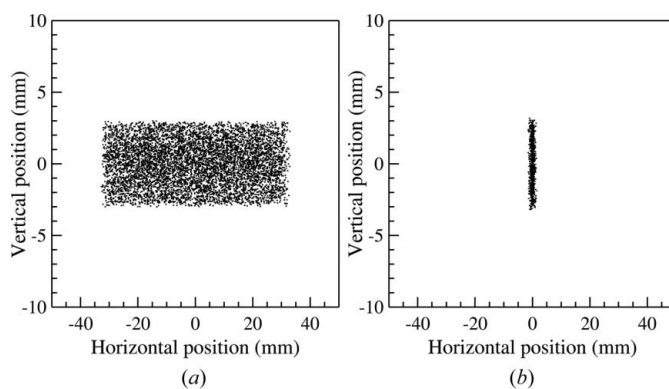
3.3. Mirror

The function of the vertical beam optic is to re-condition the vertical monochromatic beam coming out of the DLM and to adapt the two operation modes of XPD by focusing or collimating the beam, respectively. The compound refractive lenses (CRLs) and the mirror are both suitable for the energy tunability requirement of the XPD beamline. However, a significant drawback of the CRL is the aperture-limited gain in flux for long-focal-length (low demagnification) focusing. It is also difficult to match the limited hole depth of the CRL with the large horizontal size of the beam (about 24 mm wide at the optic location with the DLM focusing the beam horizontally at the sample position).

The mirror is therefore the best choice for high-energy beamlines using wiggler sources. The XPD platinum-coated mirror provides high reflectivity for high energies from 30 keV to 70 keV with the optimized grazing angle, δ [*cf.* Fig. 9(*a*)]. Ideally, the point-to-point focusing requires an elliptical bending of the mirror in the meridional direction while the collimating mode requires a parabolic bending. However, the
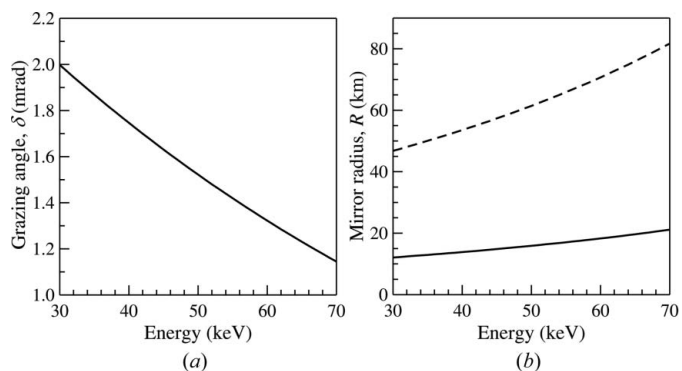

Figure 9
(*a*) Maximum grazing angles to ensure a reflectivity over 90% plotted as a function of photon energies for a Pt-coated mirror with 0.2 nm r.m.s. roughness, calculated by *XOP*. (*b*) The cylindrical bending radii of the focusing (solid line) and collimating (dashed line) mirror, calculated from equation (6), plotted as a function of photon energies.

coma and spherical aberrations of the XPD mirror are negligible owing to the large focal length. Careful ray-tracing verification was performed to prove the adequacy of utilizing a cylindrically bent mirror. The meridional bending radius R is calculated from

$$\frac{1}{p + F_1(\gamma_H^2/\gamma_0^2 - 1)} + \frac{1}{q} = \frac{2}{R \sin \delta}, \qquad (6)$$

with the source-to-mirror distance $p = 40.1$ m and the mirror-to-sample distance $q = 16.3$ m for the focusing mode and $q = \infty$ for the collimating mode. (Note that the virtual source-to-mirror distance is modified as discussed in §3.2.2.) Fig. 9(b) presents the required bending radii as a function of the photon energies calculated from (6) with the optimized grazing angle shown in Fig. 9(a).

The performance of the mirror is also determined by the roughness and the slope error. The surface roughness, characterized by the r.m.s. value of the surface height variation, affects the mirror reflectivity by means of diffuse scattering (diffraction). For the mirror at the XPD beamline, a roughness of 0.2 nm will be sufficient to maintain 90% reflectivity at the optimized angles [cf. Fig. 9(a)] for the whole energy range. Another effect of the roughness is to generate a diffuse scattering background, which has a slightly larger size than the spot size that is obtained without considering the mirror roughness. This scattering background is detrimental to imaging, but not as important for powder diffraction. In the paper, the modeling of the roughness in the ray tracing is not applied for obtaining the beam profile. The roughness is only used to calculate the total reflectivity of the mirror and the corresponding beam flux.

On the other hand, the slope error ($\sigma_{r.m.s.}$), defined as the r.m.s. value of the angular variation from the ideal shape, is more critical for determining the beam size in the high-flux mode and the energy bandwidth in the high-resolution mode. Fig. 10 shows these effects from the mirror with different slope errors simulated in *SHADOW*, where the surface profiles are generated by the *WAVINESS* subroutine for a mirror that is 1.3 m long and 5 cm wide. Considering that the effective

vertical source size is 28 µm (r.m.s.) at 50 keV [cf. Fig. 4(b) and text in §3.1] and the demagnification factor of the mirror is about 1:2.5, the focal size should be around 11 µm (r.m.s.) for an ideal mirror. However, the ray tracing shows a focal size of 18 µm r.m.s. ($s_{v0} = 38$ µm FWHM) with zero slope error applied on the mirror [cf. Fig. 10(a)]. This value can only be obtained by implementing the DLM simulation mentioned in §3.2.2. Once this blurring effect of the DLM is included in determining s_{v0}, the real FWHM vertical beam size, s_v, can be obtained from *SHADOW* ray tracing [markers in Fig. 10(a)] or calculated analytically by convoluting the contribution of the slope error [solid line in Fig. 10(a)], given by

$$s_v = \left[s_{v0}^2 + 4(2.355\sigma_{r.m.s.}q)^2\right]^{1/2}. \qquad (7)$$

Similarly, Fig. 10(b) illustrates the energy resolution plotted as a function of $\sigma_{r.m.s.}$ when combining the collimating mirror with the high-resolution monochromator. The FWHMs of $\Delta E/E$ extracted from *SHADOW* ray tracing [markers in Fig. 10(b)] agree with those calculated by [solid line in Fig. 10(b)]

$$\Delta E/E = \left[\omega + 4(2.355\sigma_{r.m.s.})^2\right]^{1/2} / \tan \theta_m, \qquad (8)$$

where ω is the intrinsic angular acceptance of the HRM.

4. Instrumental resolution function

The accurate description of the instrumental resolution function (IRF) is extremely important for characterizing the XPD beamline. In the high-flux set-up (cf. Fig. 1) the instrumental angular profile in the vertical plane is a convolution of the incident beam profile, the rocking curve of the Laue crystal monochromator, the slit (located before the VFM) function, the residual divergence after the focusing mirror, and the angular acceptance of the detector, with α_m, Δ_m, τ_s, τ_f and τ_d as their Gaussian FWHMs, respectively. The FWHM of the IRF as a function of the diffraction angle θ is deduced by means of an analytical method (Sabine, 1987; Gozzo *et al.*, 2006), given by

$$\Delta_{HF}^2(2\theta) = 4k^2 m_s^2 \alpha_m^2 \tau_s^2/(\alpha_m^2 + \tau_s^2) + 2m_s^2 \Delta_m^2 + \tau_f^2 + \tau_d^2, \qquad (9)$$

with

$$k = 1 - F_1/\left[R_m \cos(\chi \pm \theta_m)\right],$$
$$m_s = \tan \theta / \tan \theta_m.$$

The parameter k accounts for the mismatching of the meridional bending radius R_m of the DLM crystals and the source-to-DLM distance F_1 (*e.g.* $k = 0$ for the Rowland geometry and $k = 1$ for flat Laue crystals). It is clear that the slit after the DLM serves as the regulation of the incident beam divergence through the term $\alpha_m^2 \tau_s^2/(\alpha_m^2 + \tau_s^2)$, which reduces to α_m^2 when the slit is widely open ($\tau_s = \infty$). In most of the high-throughput experiments, area detectors are preferred without utilizing the analyzer crystals in order to achieve the fast detection.

In the high-resolution set-up (cf. Fig. 1), it is assumed that the rocking curve width (Δ_m) of the DLM and the mirror acceptance (τ_s) are much larger than that of the channel-cut
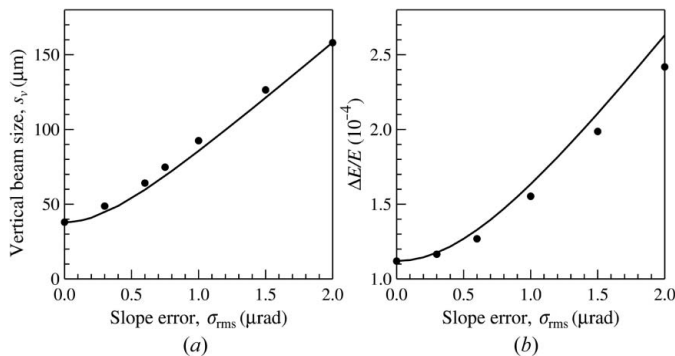

Figure 10
Vertical beam size (a) in the high-flux mode and the energy resolution (b) in the high-resolution mode plotted as a function of the slope error of the VFM. The markers are ray-tracing results using *SHADOW* and the lines are calculated analytically. See text for details.
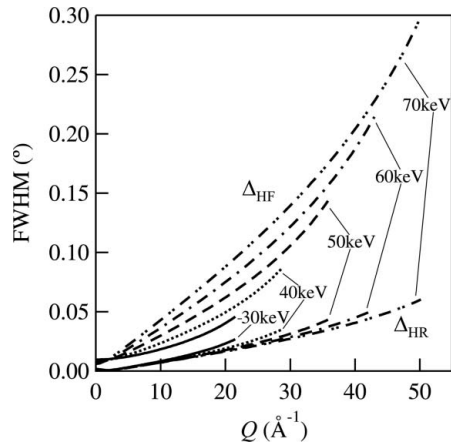
research papers

Figure 11
Instrumental resolution plotted as a function of Q at different energies (30 keV, 40 keV, 50 keV, 60 keV and 70 keV) in the high-flux mode (Δ_{HF}) and the high-resolution mode (Δ_{HR}), calculated from equations (9) and (10), respectively. The input parameters for the calculations are listed in Table 2.

HRM (Δ_c) and the analyzer crystal (Δ_a). It is also assumed that Δ_m and τ_s are much larger than the residual divergence of the collimated beam (τ_f) after the mirror. The FWHM of the high-resolution IRF is then

$$\Delta_{HR}^2(2\theta) = (b + m_c)^2 \tau_f^2/m_c^2 + b^2 \Delta_c^2/(2m_c^2) + \Delta_a^2, \qquad (10)$$

with

$$b = \tan\theta_a/\tan\theta_m - 2\tan\theta/\tan\theta_m,$$
$$m_c = \tan\theta_c/\tan\theta_m,$$

where θ_c and θ_a are the Bragg angles of the HRM crystals and the analyzer crystal, respectively.

Fig. 11 shows the instrumental resolution as a function of Q in the reciprocal space [$Q = (4\pi\sin\theta/\lambda)$, λ is the X-ray wavelength] at different energies in the high-flux mode and the high-resolution mode calculated from (9) and (10), respectively. The values of the profile FWHMs of the optics for the XPD beamline are listed in Table 2. The incident beam divergence α_m is determined by the fixed mask aperture. Δ_m is calculated analytically from (3) and (4). τ_s is taken as the vertical angular acceptance of the mirror after the DLM [$\tau_s = L\sin\delta/p$, with the mirror length $L = 1.3$ m and the grazing angle δ from Fig. 9(a)] and τ_f is given by $L\sin\delta/q$. In the high-resolution mode, τ_f is assumed to be 15 µrad (Gozzo *et al.*, 2006). Δ_a and Δ_c are calculated using the dynamical theory for the silicon 111 reflection in symmetric Bragg geometry. The energy resolution at 30 keV is comparable with existing high-resolution powder diffraction beamlines (Gozzo *et al.*, 2006; Masson *et al.*, 2001; Wang *et al.*, 2008), which are all optimized for energies below 40 keV.

5. Discussion

Table 3 lists the *SHADOW* ray-tracing results for the XPD beamline in both the high-flux mode and the high-resolution mode. The calculation parameters are from Table 1, Table 2

Table 2
Values of the profile FWHM of the optics and parameters needed to generate Fig. 11 using equations (9) and (10) in §4.

Energy, E (keV)	70	60	50	40	30
Bragg angles, θ_m, θ_c, θ_a (°)	1.62	1.89	2.27	2.83	3.78
DLM sagittal radius, R_s (m)	0.886	1.04	1.25	1.57	2.09
DLM meridional radius, R_m (m)	25.0	27.1	30.1	34.6	42.1
VFM grazing angle, δ (mrad)	1.14	1.32	1.52	1.75	2.00
α_m (µrad)†	100	100	100	100	100
Δ_m (µrad)†	99.6	82.7	66.4	50.9	36.5
τ_s (µrad)†	37.0	42.8	49.3	56.7	64.8
τ_f (µrad), focusing†	90.9	105	121	140	160
τ_d (µrad)†	50	50	50	50	50
τ_f (µrad), collimating†	15.0	15.0	15.0	15.0	15.0
Δ_a, Δ_c (µrad)†	4.00	4.66	5.60	7.01	9.37

† α_m, Δ_m, τ_s, τ_f, τ_d, Δ_a and Δ_c are the FWHMs of the incident beam profile, the rocking curve of the Laue crystal monochromator, the slit (located before the VFM) function, the residual divergence after the VFM, the angular acceptance of the detector, the rocking curve of the HRM and the rocking curve of the analyzer crystal, respectively.

and Fig. 9. The r.m.s. slope error of the Pt-coated mirror is assumed to be 0.5 µrad and the roughness is 0.2 nm. The total fluxes at the sample were calculated from

$$\mathcal{F} = \frac{\mathcal{F}_0 N_f \Delta E_i}{0.001 N_i E}, \qquad (11)$$

where $\mathcal{F}_0$ is the total incident flux [photons s^{-1} (0.1% bandwidth)$^{-1}$] after the fixed aperture mask and the filter system (2 mm of diamond and 4.8 mm of SiC), N_i is the number of initial rays, N_f is the number of final rays at the sample location recorded by *SHADOW*, ΔE_i is the input photon energy bandwidth over which the ray tracing is performed, and E is the central photon energy. The output energy bandwidth, ΔE, is obtained by fitting the intensity-weighted energy histogram from the *SHADOW* output.

The simulation results indicate an optimized photon flux at the sample around 50 keV. The beam size and flux numbers, however, cannot be described in a simple pattern owing to the complexity introduced by the DLM. Ideally, the anticlastic bending radii (R_m) of both crystals are the same for the same crystal shape and size. However, they also depend on the bending mechanism, the bender manufacturing error and, most importantly, the heat load. Since the first crystal operates under the white beam and extreme cooling (liquid nitrogen), the resulting R_{m1} will vary from that of the second crystal (R_{m2}).

Fig. 12 shows the relative flux per energy bandwidth at 50 keV with different R_{m1} and R_{m2} combinations keeping R_{s1} and R_{s2} constant (1.25 m), from which the optimized bending conditions for both crystals can be obtained. Note that each point on the surface is extracted from the ray tracing using the multi-lamellar model described in §3.2.2. As a result, it is important to have a simple adjustment of the meridional bending radius while the sagittal radius is pre-determined from the focusing condition. Previous studies (Shi *et al.*, 2011) show that the R_s/R_m ratio varies with the crystal shape (*i.e.* the aspect ratio). The XPD beamline intends to use a four-bar bender design where the spacing between the inner bars is adjustable. The actual bending of the crystal changes under the effect of the thermal load. Tuning the inner bar spacing can

Table 3
Beamline performance simulated by *SHADOW* ray tracing.

E (keV)	70	60	50	40	30
Incident flux, $\mathcal{F}_0$ [10^{12} photons s^{-1} (0.1% bandwidth)$^{-1}$]†	16	33	62	93	78
High-flux mode					
$\Delta E/E$ (10^{-3})	2.3	1.6	0.99	0.59	0.40
Beam size, $s_h \times s_v$ (mm)	0.78×0.064	0.64×0.055	0.61×0.057	0.81×0.060	0.71×0.080
Flux, $\mathcal{F}$ (10^{12} photons s^{-1})	4.4	8.9	17	19	12
Intensity, I (10^{14} photons s^{-1} mm^{-2})	0.89	2.5	4.9	3.9	2.2
Intensity gain‡	25	35	50	30	35
High-resolution mode					
$\Delta E/E$ (10^{-3})	0.14	0.13	0.12	0.12	0.10
Beam size, $s_h \times s_v$ (m)	0.64×1.5	0.72×1.7	0.80×2.0	0.65×2.3	0.65×2.6
Flux, $\mathcal{F}$ (10^{12} photons s^{-1})	0.20	0.69	1.8	3.7	2.6
Intensity, I (10^{12} photons s^{-1} mm^{-2})	0.21	0.56	1.2	2.5	1.5

† Flux after the fixed aperture mask and the filter system (2 mm of diamond and 4.8 mm of SiC). ‡ Intensity per bandwidth [photons s^{-1} mm^{-2} (0.1% bandwidth)$^{-1}$] ratio between the high-flux mode and the high-resolution mode.
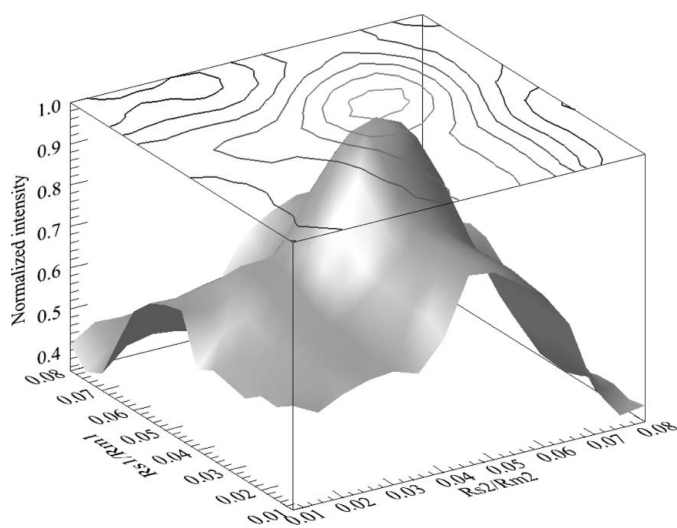

Figure 12
Normalized flux per energy bandwidth at 50 keV plotted as a function of the radius ratio R_{s1}/R_{m1} and R_{s2}/R_{m2} of the two DLM crystals, where the R_s values are fixed (1.25 m) to satisfy the focusing condition and only the R_m values vary. The fluxes and energy bandwidths are extracted from the *SHADOW* ray tracing using the multi-lamellar model of the DLM crystals.

minimize this change and therefore ensures the optimization of the output flux (*e.g.* at the peak position as shown in Fig. 12).

6. Conclusion

The performance of the X-ray Powder Diffraction beamline at NSLS-II is simulated using the *SHADOW* ray tracing. The major design challenge relies on the simulation of the DLM, of which the unique features have a huge impact on the design of the downstream optics (*i.e.* the VFM) and dominate the final performance of the beamline. In this paper we proposed a multi-lamellar model to reveal the optical characteristics of the DLM in the ray-tracing process. The simulations show that the expected beamline performance will serve the proposed scientific objectives. Based on the present analysis, the XPD beamline is designed to deliver high fluxes at the sample in

variable millimeter-size focuses over the tunable energy range of 30 to 70 keV. The energy resolution will be 10^{-3} in the high-flux mode and up to 10^{-4} in the high-resolution mode. Future upgrades will include the secondary focus of the beam down to a size of 10 μm and the implementation of a dedicated PDF endstation.

References

Chubar, O. (2001). *Proc. SPIE*, **4143**, 48–60.
Drakopoulos, M. (2010). Private communication.
Gozzo, F., De Caro, L., Giannini, C., Guagliardi, A., Schmitt, B. & Prodi, A. (2006). *J. Appl. Cryst.* **39**, 347–357.
Krisch, M., Freund, A., Marot, G. & Zhang, L. (1991). *Nucl. Instrum. Methods Phys. Res. A*, **305**, 208–213.
Masson, O., Dooryhee, E., Cheary, R. W. & Fitch, A. N. (2001). *Mater. Sci. Forum*, **378–381**, 300–307.
Rumaiz, A. K., Woicik, J. C., Carini, G. A., Siddons, D. P., Cockayne, E., Huey, E., Lysaght, P. S., Fischer, D. A. & Genova, V. (2010). *Appl. Phys. Lett.* **97**, 242108.
Sabine, T. M. (1987). *J. Appl. Cryst.* **20**, 23–27.
Sanchez del Rio, M. & Dejus, R. J. (2004). *Proc. SPIE*, **5536**, 171–174.
Shi, X. (2011). *Proc. SPIE*, **8141**, 81410W.
Shi, X., Ghose, S., Zhong, Z., Rehak, M. L., Kaznatcheev, K., Takacs, P. Z. & Dooryhee, E. (2011). *J. Appl. Cryst.* **44**, 665–671.
Suortti, P., Thomlinson, W., Chapman, D., Gmür, N., Greene, R. & Lazarz, N. (1990). *Nucl. Instrum. Methods Phys. Res. A*, **297**, 268–274.
Wang, J., Toby, B. H., Lee, P. L., Ribaud, L., Antao, S. M., Kurtz, C., Ramanathan, M., Von Dreele, R. B. & Beno, M. A. (2008). *Rev. Sci. Instrum.* **79**, 085105.
Welnak, C., Chen, G. J. & Cerrina, F. (1994). *Nucl. Instrum. Methods Phys. Res. A*, **347**, 344–347.
Wortman, J. J. & Evans, R. A. (1965). *J. Appl. Phys.* **36**, 153–156.

Zhong, Z., Kao, C. C., Siddons, D. P. & Hastings, J. B. (2001a). *J. Appl. Cryst.* **34**, 504–509.

Zhong, Z., Kao, C. C., Siddons, D. P. & Hastings, J. B. (2001b). *J. Appl. Cryst.* **34**, 646–653.

Zhong, Z., Kao, C. C., Siddons, D. P. & Hastings, J. B. (2002). *Acta Cryst.* A**58**, 487–493.

Zhong, Z., Kao, C. C., Siddons, D. P., Zhong, H. & Hastings, J. B. (2003). *Acta Cryst.* A**59**, 1–6.